Heat and mass transfer implications of droplet injection in a riser system

Chemical Engineering Science 304 (2025) 121066

Contents lists available at ScienceDirect

Chemical Engineering Science

journal homepage: www.elsevier.com/locate/ces

Heat and mass transfer implications of droplet injection in a riser system – a CFD-DEM approach

Juan G. Ramírez, Frank de Konink, Vivekanand Swami, Maike Baltussen *, Kay Buist, Johannes A.M. (Hans) Kuipers

Multiphase Reactors Group, Department of Chemical Engineering & Chemistry, Eindhoven University of Technology, Eindhoven, 5600 MB, The Netherlands

ARTICLE INFO

Keywords:
Coupled heat and mass transfer
CFD-DEM
Evaporation rate
Experimental validation
Riser

ABSTRACT

In risers, important catalytic processes occur which benefit from the intensive heat and mass transfer in this type of reactor. Typically the reactants are introduced in the liquid phase in the form of small droplets which rapidly evaporate. In this work the effect of this evaporation on the heat and mass transfer is studied using a computational fluid dynamics-discrete element method approach, treating the gas as a continuous phase and the particles and injected liquid as discrete elements. The closures for particle-droplet interaction were obtained from advanced DNS computations reported in literature. The simulations are validated with experiments conducted using air, glass beads and water in a pseudo-2D riser with dimensions 1.57 m x 0.07 m x 0.0065 m. The results indicate that under the experimental conditions (fast fluidization regime and temperatures between 20 °C and 150 °C), evaporation primarily occurs from the liquid deposited on the particles surface. Significant radial gradients in water vapor concentration prevail, with high concentrations near the wall close to the nozzle. The overall thermal behavior, including asymmetries in the radial profiles, is driven by the strong solids circulation in the bottom section of the riser.

1. Introduction

Riser reactors play an important role in the chemical industry for conducting catalytic process such as gasification, base chemical production and Fluid Catalytic Cracking (FCC). These reactors typically have a simple design: a tall reactor in which catalyst particles are injected from the bottom along with the gas that conveys the particles. At the exit of the riser, the gas and the particles are separated using a cyclone. The feedstock can be introduced as a gas as well as in the form of micron-sized droplets, which are introduced through the side wall of the reactor using multiple nozzles (Shah et al., 2016). These droplets evaporate due to the high temperatures inside the riser, and subsequently react with the catalyst. It is often assumed that this evaporation occurs instantaneously after injection of the liquid. However, there are multiple factors influencing the evaporation rate including droplet size, temperature, gas velocity, chemical composition. Consequently, the evaporation rate can range from a few milliseconds to several seconds (Buchanan, 1994), which is comparable to the residence time of the catalyst within the riser. If the evaporation is not instantaneous liquid droplets will exist for long periods of time inside the riser. This means that the solid catalyst particles will become wet after collision with droplets, affecting its collision behavior as well as the effective evaporation rate.

To model the evaporation of the droplets and the complex interactions of this three-phase gas-liquid-solid flow inside a riser requires a few key considerations are necessary. The first consideration is regarding the representation of each phase. The gas is typically modeled as a continuous phase and simulated with Computational Fluid Dynamics (CFD). On the other hand, the particles and droplets can be either represented as continuous phases or individually tracked using the Discrete Element Method (DEM). In previous studies on the modeling of this gas-liquid-solid flows including evaporation, the particles and droplet have been considered to be a continuous phase, which is cpu-efficient but limits the accuracy in predicting the evaporation characteristics (Gao et al., 2001; Lopes et al., 2012; Theologos et al., 1999; Gupta and Subba Rao, 2001). This limit in the accuracy is caused by the inability of the model to include the contribution of the collision of droplets and hot particles on the evaporation (Buchanan, 1994). To accurately capture this significant contribution, each particle-droplet encounter should be tracked individually. Therefore, this work focuses on the treatment of both the droplets and particles as discrete elements.

* Corresponding author.
E-mail address: m.w.baltussen@tue.nl (M.W. Baltussen).

https://doi.org/10.1016/j.ces.2024.121066
Received 26 August 2024; Received in revised form 11 November 2024; Accepted 6 December 2024

Available online 11 December 2024

Nomenclature

Roman symbols

a	shape parameter of Weibull radius distribution	
b	scale parameter of Weibull radius distribution	
$C_{p,a}$	particle or droplet heat capacity	J/kg K
$C_{p,g}$	gas heat capacity	J/kg K
d_p	particle diameter	m
e_n	normal restitution coefficient	
e_t	tangential restitution coefficient	
h_g	inter-phase heat transfer coefficient	$W/m^2 K$
$h_{f,g}$	specific latent heat of evaporation	J/kg
H_g	gas specific enthalpy	J/kg
$\mathbf{g}$	gravity	m/s^2
G_s	solids flux	$kg/m^2 s$
$\mathbf{I}_a$	particle or droplet moment of inertia	$kg\,m^2$
m_a	particle or droplet mass	kg
m_p	particle mass	kg
P	pressure	Pa
Re	particle Reynolds number	
R_p	particle radius	m
$\mathbf{r}_p$	particle position	m
S_h	heat transfer source term	W/m^3
S_m	mass transfer source term	1/s
$\mathbf{S}_u$	momentum transfer source term	N/m^3
t	time	s
$\mathbf{T}_a$	particle or droplet torque	N m
T_g	gas temperature	K
$\mathbf{u}_g$	gas velocity	m/s
$\mathbf{U}$	superficial slip velocity	m/s
$\mathbf{v}_p$	particle velocity	m/s
$\mathbf{V}_a$	particle or droplet volume	m^3
V_{cell}	Eulerian cell volume	m^3
w_g	moisture mass fraction	
w_g^*	moisture mass fraction at the surface of the droplet or the wet particle	
x/W	dimensionless riser width	

Greek symbols

β	inter-phase momentum transfer coefficient	$kg/(m^3 s)$
γ_{nozzle}	secondary angle of the flat nozzle spray	°
δ_l	thickness of the liquid film on the particle surface	m
ε_g	gas volume fraction	
θ_{nozzle}	main angle of the flat nozzle spray	°
μ	gas viscosity	kg/(m s)
μ_{fr}	dynamic friction coefficient	
μ_{nozzle}	mean velocity of droplets leaving the nozzle	m/s
ρ_g	gas density	kg/m^3
ρ_p	particle density	kg/m^3
σ	liquid surface tension	N/m
σ_{nozzle}	standard deviation of droplets velocity leaving the nozzle	m/s
φ	fraction of particle surface covered with liquid	
ϕ_s	solids volume fraction	
$\boldsymbol{\tau}_g$	stress tensor	Pa
ω_a	particle or droplet angular velocity	s^{-1}

For the evaporation during particle-droplet collision, Buchanan et al. (Buchanan, 1994) proposed theoretical limits for the evaporation rate: 1) the thermal energy transfer during collision is infinitely fast and 2) the transfer occurs over a finite collision time. In these limits, the preceding particle-droplet collision outcome is not considered, e.g. the wetting of the particle or splashing of the droplet. These collision outcomes will affect the effective mechanism of the evaporation. Therefore, our model will include the formation of the liquid layer on the particle or the splashing behavior depending on the Weber number of the collision.

Besides the numerical approaches, the evaporation has been studied experimentally (Gehrke and Wirth, 2007; Gao et al., 2001; Gupta and Subba Rao, 2001; Fan et al., 2001). However, most of this data is limited to point measurements at the riser outlet and involves variables that contain multiple phenomena, e.g. the global reactor yield (Gao et al., 2001; Gupta and Subba Rao, 2001). This makes it challenging to assess the accuracy of any model specifically regarding the precise role of evaporation.

To determine the validity of the developed model, an experimental setup has been developed, which enables the measurement of relevant parameters of evaporation, e.g. temperature and relative humidity, alongside the detailed information on solids distribution and flux. Gehrke and Wirth (2007) performed a similar study on liquid evaporation in a high density riser. However, their study involved very high solids flux and liquid flow rates, which is unfeasible to reproduce with the detailed DEM approach for particles and droplets. The number of particles and droplets are one to two orders of magnitude lower in the proposed setup, allowing us to perform a one-to-one comparison in terms of solids dynamics and relevant heat and mass transfer variables. Fan et al. (2001) evaluated the evaporation of liquid nitrogen in a dilute riser, however, the extremely high vapor pressure of nitrogen significantly reduces the lifetime of the droplets leading to near instantaneous evaporation. In this work the vapor pressure is lower, which means that a large part of the liquid will come into contact with the particles and evaporation also occurs from liquid attached to the solid surface.

This paper will first describe the CFD-DEM approach, with a focus on the treatment of heat and mass transfer and the verification of the model. The details of the experimental setup are provided. Afterwards, the methods section concludes with the used simulation conditions. The results section examines the impact of water on the solids distribution within the riser without evaporation. Secondly, the evaporation rate is evaluated and compared with experimental data in terms of relative humidity. Finally, the analysis explores the gas and solid temperatures along the riser stressing the interplay between heat transfer and solids circulation.

2. Methods

This section outlines the combined modeling and experimental approaches used in this study. First, the CFD-DEM model is described for a system involving gas, particles, and droplets, along with the performed verification, which focuses on the heat and mass transfer between the phases. Next, the experimental riser setup is discussed. Finally, the simulation settings for the CFD-DEM representation of the riser are detailed.

2.1. Computational Fluid Dynamics-Discrete Element Method (CFD-DEM)

2.1.1. Gas phase motion

The CFD-DEM in this work is based on the formulations developed for gas-solid systems (Tsuji et al., 1998; Hoomans et al., 1996). The model considers the gas in the riser as a continuous phase, which is described by the volume-averaged Navier-Stokes equations and the continuity equation (equations (1) and (2), respectively).

$$\frac{\partial(\varepsilon_g \rho_g \mathbf{u}_g)}{\partial t} + \nabla \cdot (\varepsilon_g \rho_g \mathbf{u}_g \mathbf{u}_g) = -\varepsilon_g \nabla P - \nabla \cdot (\varepsilon_g \boldsymbol{\tau}_g) - \mathbf{S}_u + \varepsilon_g \rho_g \mathbf{g} \quad (1)$$

$$\frac{\partial(\varepsilon_g \rho_g)}{\partial t} + \nabla \cdot (\varepsilon_g \rho_g \mathbf{u}_g) = 0 \quad (2)$$

Where $\mathbf{S}_u$ represents the source term due to the momentum transfer between the gas and both particles and droplets:

$$\mathbf{S}_u = \frac{1}{V_{cell}} \sum_{i=1}^{N_p+N_d} \frac{\beta V_a}{1-\varepsilon_g}(\mathbf{u}_g - \mathbf{v}_a)\delta(\mathbf{r}-\mathbf{r}_a) \tag{3}$$

$\delta(\mathbf{r}-\mathbf{r}_a)$ is the regularized Dirac delta function, which maps the source term for each of the particles ($a=p$) and droplets ($a=d$) to the relevant Eulerian grid cells. This same delta function maps the gas phase properties and velocities from the Eulerian grid to the particles and droplets position. β is the inter-phase momentum transfer coefficient computed with the correlation proposed by Tang et al. (2015), which accurately predicts the experimental data of this riser system (Ramírez et al., 2023). While it is true that the drag correlation used was developed from particle-resolved simulations of gas solid systems, Sutkar et al. (2016) showed that assuming that both particles and droplets to be (semi)rigid objects give good predictions in simulations of gas-particle-droplet systems provided that the droplets can be considered as rigid, which constitutes a good approximation for very small droplets.

In principle, both Equation (1) and Equation (2) should include a source term contribution due to the liquid evaporation, however under the dilute conditions considered here (see section 2.3 for details), this contribution can be neglected as the force density of the most important terms in the momentum equation ($-\varepsilon_g \nabla P - \mathbf{S}_u$) are on average ~ 40 times higher compared to the contribution of the evaporation.

2.1.2. Particle and droplet motion

The motion of both discrete phases, particles and droplets, is described using Newton's second law of motion:

$$m_a \frac{d^2\mathbf{r}_a}{dt^2} = \frac{\beta V_a}{1-\varepsilon_g}(\mathbf{u}_g - \mathbf{v}_a) - V_a \nabla P + m_a \mathbf{g} + \mathbf{F}_{\text{contact},a} \tag{4}$$

The last term of the RHS is only considered for the particles and accounts for the collisions with other particles and walls. The collisions between particles and droplets require a special treatment, which is explained in section 2.1.3. Particle-particle and particle-wall collisions are treated with the soft sphere approach based on a linear spring-dashpot representation (Cundall and Strack, 1979). However, some of the particles might be (partially) wet due to the interaction with droplets. In these (partially) wet collisions, the capillary and viscous effects should be included (see Section 2.1.3 for the inclusion of these effects). Collisions between droplets are not considered in this work as the droplet-to-particle size ratio is small ($< 1/15$). Also, droplets that hit the walls of the system are immediately removed from the domain. The conservation of linear momentum for the droplets should ideally involve a more complex approach than shown in Equation (4), due to the mass change caused by evaporation. However, as discussed in section 3.2, the liquid droplets in this system will collide with a particle or a wall before significant evaporation occurs.

For the particles, the conservation of angular momentum is also included to obtain the rotational velocities of the particles:

$$\mathbf{I}_a \frac{d\omega_a}{dt} = \mathbf{T}_a \tag{5}$$

2.1.3. Particle-droplet collision

For the collisions between particles and droplets we use the same approach as in our previous work (Ramírez et al., 2024), of which a short explanation is provided here. When a particle and droplet collide, there are multiple possible outcomes e.g., partial or total deposition, rebound, complete coating and splashing. In this research, the closure for particle-droplet interaction, represented by collision outcome maps, is obtained from advanced DNS computations of Yoon and Shin (2021). The selected particles have a hydrophilic surface (low contact angle) and the droplet-to-particle size ratio is small (see Section 2.3 for further details), limiting the number of possibilities for the collisions to coating and splashing. Whether the collision outcome is coating or splashing is defined based on the Weber number $\left(We = \frac{\rho_d v_{rel}^2 d_d}{\sigma}\right)$. All collisions occurring with a low Weber number ($We \leq 170$) result in coating of the entire droplet volume on the particle surface. For splashing ($We > 170$), only 20% of the droplet volume remains at the particle surface. The rest of the droplet volume creates satellite droplets, which are assumed to directly evaporate to reduce the computational time. Due to the momentum exchange during the particle-droplet collision, the particle will experience a change in its velocity, which can be obtained with Equation (6). Note that f_{dep} accounts for the fraction of the droplet deposited on the particle surface, i.e., 1.0 if the result of collision is particle coating and 0.2 if it is splashing. Furthermore, it is assumed that the angular velocity is unaffected by the particle-droplet collision.

$$\mathbf{v}_p' = \frac{m_p \mathbf{v_p} + f_{dep} m_d \mathbf{v_d}}{m_p + f_{dep} m_d} \tag{6}$$

One important variable to track with particle-droplet collisions is the fraction of particle surface covered with liquid. This is accomplished with the variable (φ) assigned to each particle of the system and varies between 0 and 1. When a droplet deposits on a particle, the change in coverage fraction, $\Delta\varphi$, is computed on basis of the equilibrium position of the liquid (Patel et al., 2017). When multiple droplets collide with a particle, the contributions of the different droplets should be combined. In this research we assume that droplets hit randomly any spot of the particle, whether it is a dry or wet spot. However, the chance of hitting a dry part of the particle decreases with previous depositions of previous droplets. In this work, the implementation of this deposition is based on the work of Kariuki et al. (2013), with a slight modification to enable handling of droplets with different sizes (see Equation (7)).

$$\varphi = 1 - \left[\prod_{i=1}^{N_{coll}} (1 - \Delta\varphi_i)\right] \tag{7}$$

This coverage will be used to determine the possibility of having a wet-wet, wet-dry or dry-dry collision between two partially wet particles. The thickness of the liquid film on the particle surface is monitored as this affects the collision properties. Although there might be high spatial variability of the thickness as a result of a non-uniform wetting (Ben and Wassgren, 2010), the liquid layer is assumed to be uniform for a particle to reduce computational expenses and is calculated using the liquid coverage and Equation (8).

$$\delta_l = \sqrt[3]{\frac{3V_{dep}}{2\pi(1-\cos\theta_w)} + R_p^3} - R_p \qquad \text{with} \quad \cos\theta_w = 1 - 2\varphi \tag{8}$$

During the collision of wet particles, there is additional energy dissipated due to viscous and capillary forces of the liquid layer. One way to represent this is by computing the collision using a wet restitution coefficient, e_{wet}, instead of the conventional dry restitution coefficient. This new parameter is computed based on energy balances during the different stages of a wet collision, resulting in a combination of algebraic expressions (Shabanian et al., 2020; Sutkar et al., 2015). In this research we implemented the approaches developed by Shabanian et al. (2020) and Sutkar et al. (2015) for particle-particle and particle-wall collisions, respectively.

2.1.4. Gas phase heat and mass transfer

The energy balance of the continuous phase is given in Equation (9).

$$\frac{\partial(\varepsilon_g \rho_g H_g)}{\partial t} + \nabla\cdot(\varepsilon_g \rho_g \mathbf{u}_g H_g) = -\nabla\cdot(\varepsilon_g \boldsymbol{q}_h) + S_h \tag{9}$$

where the variation of the specific enthalpy of the gas H_g is equal to the variation of the gas temperature T_g times the specific heat capacity of the gas at constant pressure $C_{p,g}$:

$$dH_g = C_{p,g} T_g \tag{10}$$

The heat exchange of the gas with the particles and droplets, S_h, is defined as follows:

$$S_h = \frac{1}{V_{cell}} \sum_{i=1}^{N_p+N_d} h_g A_a (T_a - T_g)\delta(\mathbf{r} - \mathbf{r}_a) \tag{11}$$

The inter-phase heat transfer coefficient, h_g, is computed using the empirical Nusselt correlation proposed by Gunn (1978).

$$\begin{aligned} Nu_a = &(7 - 10\varepsilon + 5\varepsilon^2) + [1 + 0.7 Re_a^{0.2} Sc^{0.33}] \\ &+ (1.33 - 2.4\varepsilon + 1.2\varepsilon^2) Re_a^{0.7} Pr^{0.33} \end{aligned} \tag{12}$$

where the dimensionless Nusselt and Prandtl numbers are defined as:

$$Nu_a = \frac{h_g d_a}{k_g}; Pr = \frac{\mu_g C_{p,g}}{k_g} \tag{13}$$

The conductive heat flux, $\boldsymbol{q}_h$, is computed as:

$$\boldsymbol{q}_h = -k_{eff} \nabla T_g \tag{14}$$

where k_{eff} is the effective conductivity and is given by:

$$k_{eff} = \frac{1 - \sqrt{1-\varepsilon}}{\varepsilon} k_g \tag{15}$$

The moisture mass fraction in the continuous phase is obtained by solving the species balance equation:

$$\frac{\partial(\varepsilon_g \rho_g w_g)}{\partial t} + \nabla \cdot (\varepsilon_g \rho_g \mathbf{u}_g w_g) = -\nabla \cdot (\varepsilon_g \boldsymbol{q}_m) + S_m \tag{16}$$

where $\boldsymbol{q}_m$ represents the diffusive mass flux computed as:

$$\boldsymbol{q}_m = -D_{eff,g} \nabla w_g \tag{17}$$

where $D_{eff,g}$ is the effective diffusivity which in turn depends on the moisture diffusivity in a pure gas $\left(D_{e,g}\right)$:

$$D_{eff,g} = \frac{1 - \sqrt{1-\varepsilon}}{\varepsilon} D_{e,g} \tag{18}$$

The source term, S_m, for the interfacial mass transfer from the gas phase with droplet and wet particles is computed with Equation (19).

$$S_m = \frac{1}{V_{cell}} \sum_{i=1}^{N_p+N_d} k_m A_a (w_g^* - w_g)\delta(\mathbf{r} - \mathbf{r}_a) \tag{19}$$

where w_g^* is the partial vapor content at the surface of the droplet or the liquid film when considering a wet particle. w_g^* is further discussed in Section 2.1.5. The mass transfer coefficient k_m is calculated via the Sherwood correlation proposed by Gunn (1978):

$$\begin{aligned} Sh_a = &(7 - 10\varepsilon + 5\varepsilon^2) + [1 + 0.7 Re_a^{0.2} Sc^{0.33}] \\ &+ (1.33 - 2.4\varepsilon + 1.2\varepsilon^2) Re_a^{0.7} Sc^{0.33} \end{aligned} \tag{20}$$

where the Sherwood number and Schmidt number are defined as follows:

$$Sh_a = \frac{k_m d_a}{D_{e,g}}; Sc = \frac{\mu_g}{\rho_g D_{e,g}} \tag{21}$$

2.1.5. Particle and droplet heat and mass transfer

Heat and mass transfer play an important role in this system due to the significant temperature differences between the continuous phase and the discrete elements. This heat exchange consists of both convective exchanges and the latent heat effects due to the evaporation of water from the droplets and the (partially) wet particles. In the previous section we discussed the gas phase heat and species balance. Equations (22) and (23) present the heat and mass balance for each discrete element in the system.

$$H_{f,g} \dot{m}_a + m_a C_{p,a} \frac{dT_a}{dt} = h_g A_a (T_a - T_g) \tag{22}$$

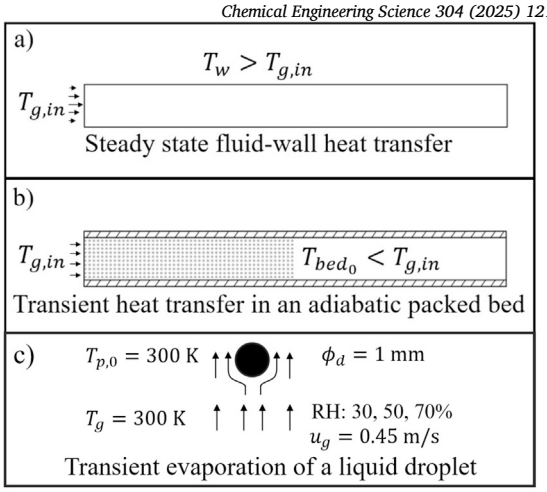

Fig. 1. Test cases for heat transfer validation.

$$\dot{m}_a = \frac{dm_a}{dt} = -k_m A_a \rho_g (w_g^* - w_g) \tag{23}$$

where $H_{f,g}$ is the specific latent heat of evaporation, and $\dot{m}_a$ the evaporation rate of the droplet or the wet particle. Equation (22) indicates that the energy required for the liquid evaporation comes from the discrete element itself, i.e., the droplet or the wet particle. For the wet particles, preliminary estimates of the heat transfer coefficient h_g (~ 100), and expected values of the liquid film thickness (< 23 μm) (Ramírez et al., 2024) suggest that no additional heat resistance is needed due to the liquid film covering the particles. w_g^* is computed with Equation (24) assuming a gas-liquid equilibrium at the interface.

$$w_g^* = \frac{P^{sat} M_d}{P M_{air}} \tag{24}$$

where P^{sat} is the saturation pressure (Pa) estimated here as a function of the temperature T (K) with the correlation proposed in the handbook of ASHRAE (see Equation (25)) (Incorporated American Society of Heating, Refrigerating & Air Conditioning Engineers, 2001).

$$\ln P^{sat} = \frac{C_8}{T} + C_9 + C_{10} T + C_{11} T^2 + C_{12} T^3 + C_{13} \ln T \tag{25}$$

with $C_8 = -5.80 \times 10^{-3}$, $C_9 = 1.39$, $C_{10} = -4.86 \times 10^{-2}$, $C_{11} = 4.18 \times 10^{-5}$, $C_{12} = -1.45 \times 10^{-8}$ and $C_{13} = 6.55$.

2.1.6. Verification

In this section, the verification of the model is discussed. This section focuses on the implementation of the coupled heat and mass transfer as the hydrodynamics has been verified and validated in previous work (Ramírez et al., 2023). Three different verification cases are discussed that verify separate aspects of the coupled model. First the implementation of the thermal energy balance of the gas phase is tested with the so-called Graetz-Nusselt problem. Secondly the heat transfer equation is checked with the heating of a packed bed of spheres and finally the combined effect of heat transfer and evaporation is checked by determining the wet bulb temperature.

- *Heat transfer in single phase flow*

  First of all the implementation of the energy equation for the continuous phase is tested by considering a laminar gas flow inside a channel at a higher constant temperature as shown in Fig. 1a. The heat exchange from the wall to the gas, represented by the Nusselt number, will continue until the fluid inside the channel reaches a thermally developed profile. Table 1 lists the simulation settings for this case. Fig. 2 shows the behavior of the Nusselt number as a function of the non-dimensional distance. It is well known that under thermally developed conditions, the Nusselt number tends to

Table 1
Simulation settings for heat transfer validation.

L(m)	0.02	$T_{g,in}$ (K)	293.15
H(m)	0.02	T_{wall} (K)	353.15
D(m)	0.2	Δt_{CFD}(s)	$5x10^{-5}$
Δx(m)	$1.0x10^{-3}$		
Δy(m)	$1.0x10^{-3}$		
Δz(m)	$2.0x10^{-3}$		

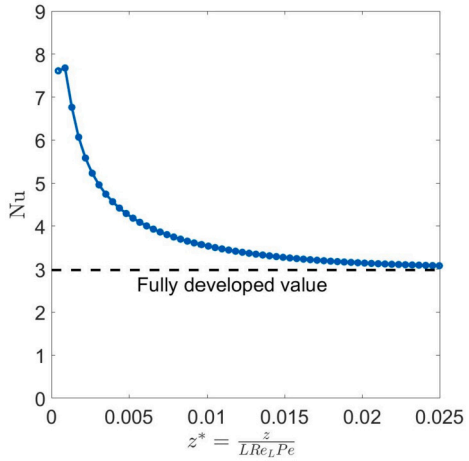

Fig. 2. Behavior of Nusselt number as a function of a non-dimensional distance in a thermally developing flow test.

an asymptotic value. The figure shows that the simulation result is reaching the value of 2.98 reported in Muzychka and Yovanovich (1998) for square tubes with isothermal walls.

- *Heat transfer in packed bed*
  Secondly the CFD-DEM implementation of heat transfer between a gas stream (continuous phase) and a discrete phase will be tested with a packed bed of particles as shown in Fig. 1b. As most of the geometrical and operational settings are the same as the previous case, Table 2 only provides the specific variables for this simulation. Results for the temperature of both the gas and solid are presented in Fig. 3 for different times and compared to an analytical solution. A sharp temperature drop in the initial section of the bed is expected during the initial seconds as reflected in Fig. 3a. Both phases clearly increase their temperature along the column over time. Finally, Fig. 3 shows a good match with the analytical results (Anzelius, 1926), indicating a correct implementation of the heat transfer between the phases.
- *Coupling of heat and mass transfer*
  To validate the simultaneous effect of heat and mass transfer in a CFD-DEM framework, the evaporation of a liquid droplet is considered when it is subjected to a gas stream with a given relative humidity (RH). During the evaporation, there are two heat transfer mechanisms: the evaporation and the heat exchange with the warmer surrounding air. When these mechanisms balance, the droplet reaches the wet bulb temperature (WBT). Fig. 1c presents the setup and settings of this simulation. The behavior of the droplet temperature is presented in Fig. 4 for three relative humidities. The results are compared with the wet bulb temperature correlation proposed by Stull (2011). Although the difference between predictions and reference values increases at lower values of relative humidity, the difference is always less than 2%.

2.2. Experimental setup

Fig. 5 presents a schematic representation of the riser setup used in this research. A detailed description of this setup in dry operation is given in Carlos Varas et al. (2017a). Therefore this description focuses on the main characteristics of the setup and the changes made to allow for the injection of droplets. The particles are injected from the downcomer Ⓑ via a dosage slit located 35 mm above the bottom of the riser. This feeding channel is inclined with an angle of 45°and its feeding rate ensures a solids flux of ~44.2 kg/m^2s. The particles travel along the riser dragged by the dry air injected from the bottom. The liquid droplets are injected by the nozzle Ⓖ located 100 mm above the bottom of the riser with an inclination of 15°.

Table 2
Simulation settings for heat transfer validation in a packed bed (check the rest of variables in Table 1).

particle array	$10 \times 10 \times 50$	$T_{g,in}$ (K)	400
d_p(m)	$1x10^{-3}$	T_{wall_i} (K)	300
ρ_p(kg/m^3)	997	T_{p_i} (K)	300
$\langle \varepsilon_g \rangle$	0.935	Δt_{DEM}(s)	$5x10^{-6}$

The biggest difference between the operation of the riser with liquid injection and the previous dry condition is that the particles that leave the cyclone Ⓒ are partially wet. To prevent wet-particles from re-entering the riser, all particles coming from the cyclone are diverted from the system using a three-way valve Ⓓ and collected in a separate vessel Ⓕ. To maintain a steady-state operation, the level of particles in the downcomer is kept constant by the injection of fresh dry particles from a storage vessel Ⓔ. A certain amount of air is injected to the downcomer from the bottom to keep the particles fluidized and ease their injection to the riser through the lateral slit. However, due to the closed valve Ⓓ during wet operation, most of this air is also entering the riser. This air stream is estimated to be ~21 l/min and included in the simulations (Section 2.3).

A heating unit Ⓗ allows for the variation of the air temperature between room temperature and 150 °C. To reduce the effect of the thick stainless steel walls of the risers on the temperature of the system, the entire system was preheated by injecting hot air at the desired temperature for approximately 2 hours (ensuring a steady state for the gas temperature at the outlet). The walls of the riser are not isolated, leading to heat losses to the ambient by natural convection, this is accounted for and discussed in the simulation strategy in section 2.3.

To insert the droplets, a pneumatic nozzle provided by Lechler (136.414.1Y.A2) was operated which injects air at 0.8 bar and a liquid flow rate of 0.25 l/h. This nozzle is designed to generate a spray pattern with a relatively planar shape. This feature was desired given the pseudo-2D nature of the used riser column. A characterization of the nozzle was performed with shadowgraphy. The major spray cone angle θ_{nozzle} was determined at 36.3° and a minor spray cone angle γ_{nozzle} of 20.3°. Measurements of the spray also included the distributions of droplet size and velocity using a Particle Image Velocimetry (PIV) technique. This nozzle characterization is disclosed in Table 3.

One of the main limitations of this setup, related to the pseudo 2D nature of the setup, was the tendency of the particles to agglomerate near the nozzle and particularly against the walls, preventing the operation in a pseudo steady state condition. To reduce the agglomeration, the solid-to-liquid mass ratio in these experiments (~290) is much larger than typical values in industrial risers (~11) (Ali et al., 1997; Derouin et al., 1997).

The pseudo-2D nature of the riser allows for detailed characterization of the solids velocity and distribution within the riser using the non-intrusive techniques: Particle Image velocity (PIV) and Digital Image Analysis (DIA), respectively. Both techniques rely on the post-processing of images taken with a high resolution camera (LaVision ImagerproHS4M, 2016 × 2016 pixels). In PIV, the mean solids velocity in a interrogation area is estimated from Equation (26) based on two consecutive frames and a cross-correlation technique.

$$\overline{v}_p(\overline{x},t) = \frac{\overline{s}_p(\overline{x},t)}{M\,\Delta t} \tag{26}$$

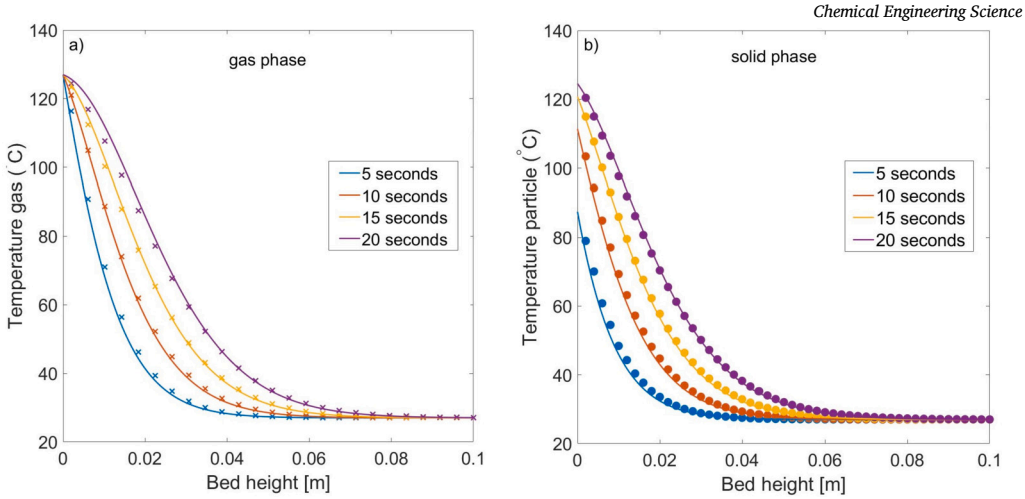

Fig. 3. Behavior of the temperature along the bed at different times for a) the gas and b) the particles for the packed bed validation test case. The lines represent the analytical solution and the symbols the simulation results.

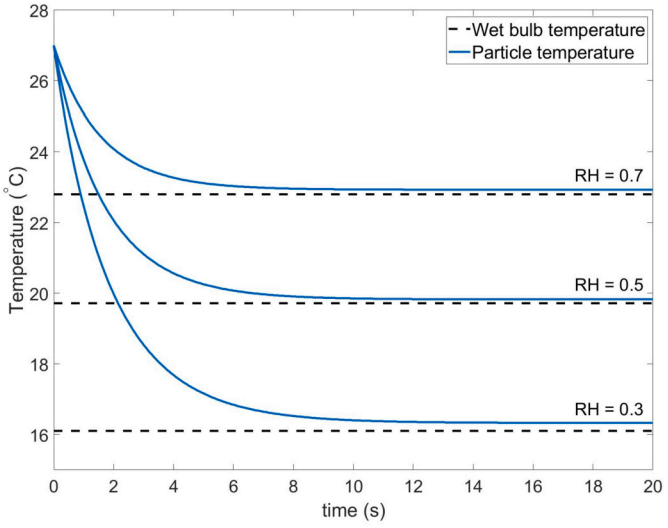

Fig. 4. Transient behavior of the droplet temperature during evaporation. Simulation results are contrasted with theoretical values.

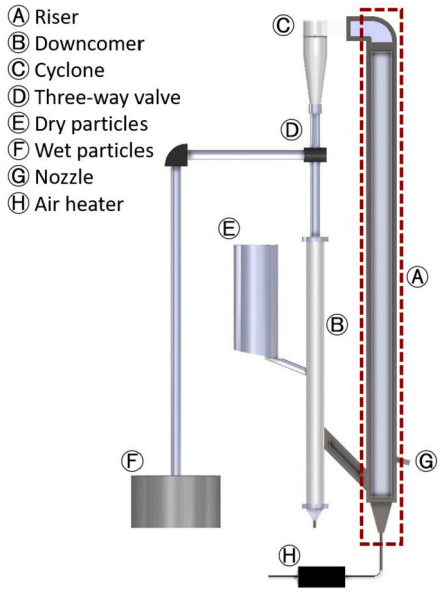

Fig. 5. The liquid coverage approaches considered in this work.

where M is the magnification factor, $\overline{v}_p(\overline{x},t)$ the solids velocity and $\overline{s}_p(\overline{x},t)$ the solids displacement in a time interval Δt. This technique is highly sensitive to the time interval between the two consecutive frames and the frequency at which these frame pairs are taken. Carlos Varas et al. (2017a) determined that 1 ms and 100 Hz, respectively, are optimal values for the riser used in this study.

The DIA technique estimates the solids distribution in the different pixels of the images using a Temporal-Histogram Method (THM). The process begins by identifying the maximum and minimum intensity values for each pixel during the whole recording. Each pixel is then normalized to compute the area covered by particles. This results in a 2D solids fraction (φ_{2D}) that can be correlated to the 3D solids fraction (φ_s) with the empirical equation below:

$$\varphi_s = AB\tanh^{-1}\left(\frac{\varphi_{2D}}{B}\right) \tag{27}$$

According to Carlos Varas et al. (2017a), the parameters A and B can be computed with equations

$$A = 0.6818 d_p/D + 0.081 f + 0.024 \tag{28}$$

$$B = 0.99 - 0.45 f \tag{29}$$

where d_p, is the particle diameter, D the thickness of the riser, and f the particle intensity fluctuation, which must be determined experimentally. For further details, see Carlos Varas et al. (2017a).

It is worth noting that there are two methods to estimate the solids flux in this setup. The first, a direct method, involves measuring the weight of the particles collected at point Ⓕ during an extended period of pseudo steady state operation. The second method estimates the solids flux using DIA/PIV measurements. It was found that the solids flux is approximately 2.7 times higher when using the DIA/PIV experiments compared to the weight measurement. These differences are caused by the inaccuracies of the solids fraction calculation with the DIA technique. Consequently, the results of solids fraction presented here will be scaled by dividing by 2.7.

2.3. Simulation conditions

In this study several different temperature conditions were studied using a constant mass flow rate, which results in different gas velocities due to the expansion of the gas. The different temperatures and respective gas velocities are listed in Table 3 along with the other relevant simulation settings.

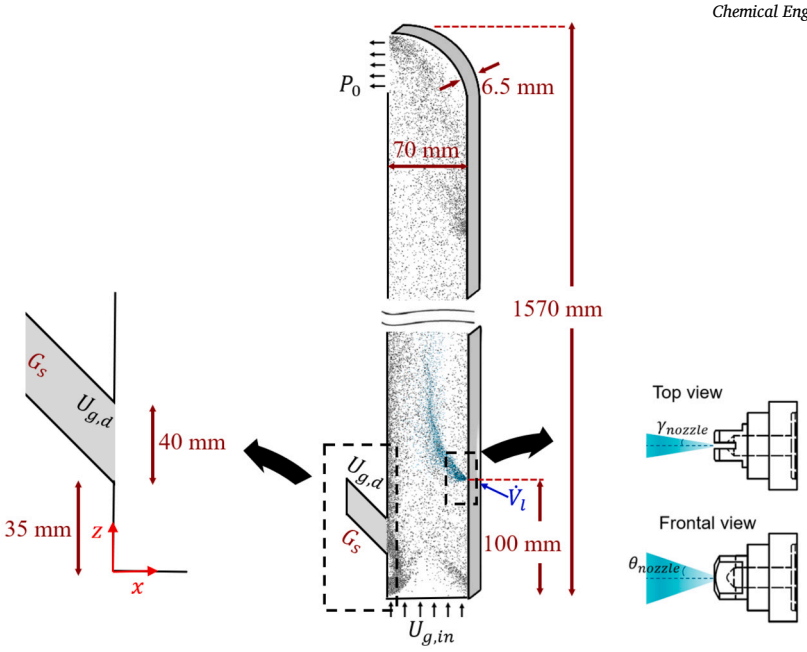

Fig. 6. Sketch of the riser to simulate.

Table 3
The simulation settings.

Setup and grid	
L(m)	0.07
D(m)	0.0065
H(m)	1.57
Δx(m)	2.5x10^{-3}
Δy(m)	1.25x10^{-3}
Δz(m)	2.5x10^{-3}
Δt_{flow}(s)	5x10^{-5}
Δt_{DEM}(s)	5x10^{-6}
Gas	
$\{T_{g,in}$(°C) $- U_{g,in}$(m/s)$\}$	{20−5.86}, {50−6.46}, {100−7.47}, {150−8.46}
$w_{g,in}$(kg/kg)	0.0
$D_{e,g}$(m^2/s)	2.42×10^{-5}
Particle	
G_s(kg/m^{2}s)	44.2
C_{p_p}(J/kg K)	840
ρ_p (kg/m^3)	2500
d_p(mm)	0.85
k_n(N/m)	1587
$e_{n_{p-p}}$	0.96
$e_{n_{p-w}}$	0.86
$\mu_{fr_{p-p}} = \mu_{fr_{p-w}}$	0.15
$e_{t_{p-p}} = e_{t_{p-w}}$	0.33
$T_{p,i}$(°C)	20
Droplets	
$T_{d,i}$(°C)	20
ΔH_{evap}(J/mol)	-40.68×10^{-3}
Flow (l/h)	0.25
Normal velocity distribution: μ_{nozzle}(m/s)	11.80
Normal velocity distribution: σ_{nozzle}(m/s)	3.68
Weibull radius distribution: shape parameter, a	1.28
Weibull radius distribution: scale parameter, b	2.08x10^{-5}
θ_{nozzle}(°)	36.3
γ_{nozzle}(°)	20.3
Nozzle inclination (°)	15

As mentioned in section 2.2, the operation of the riser is such that through the lateral slit at the left wall of the riser not only dry particles are injected but also a significant amount of air, $U_{g,d}$ in Fig. 6. A single phase CFD simulation was performed in the geometry of this small duct to obtain the velocity profile at this inlet. This velocity profile (m/s) was fitted with a fourth-degree polynomial as a function of the z coordinate (m), resulting to the following profile:

$$U_{g,d} = -3.15 \times 10^7 z^4 + 7.57 \times 10^6 z^3 - 6.59 \times 10^5 z^2 + 2.43 \times 10^4 z - 3.18 \times 10^2, \tag{30}$$

with $\left(U_{g,d}\right)_x = U_{g,d} \cos 45°$ and $\left(U_{g,d}\right)_z = -U_{g,d} \sin 45°$.

Additionally, the operation of the pneumatic nozzle used to inject the liquid droplets combines the desired liquid flow with an air stream, producing an extra contribution of air into the riser. This was estimated in ~ 9 l/min with a velocity of ~ 30 m/s. An inlet boundary condition at the right wall of the riser represents this extra air and is applied to two cells at the point of droplet injection.

The velocity of the injected particles was set to $\{0.14, 0.0, -0.14\}$ m/s. The particles are injected at a random position along 2 cm next to the left wall and 35 mm above the bottom of the riser. In case of overlap of an injected particle with a particle in the domain, the model will try new locations, if there is no position without overlap in 100 trails the simulation proceeds without particle injection until the next time step.

Although the riser walls are preheated by injecting hot gas at the desired temperature (section 2.2), they still exchange energy with the environment. Consequently, at steady state, both the gas and walls exhibit a temperature profile that decreases with the riser height. An energy balance for an element of thickness Δz results in:

$$\dot{m} C_p T\Big|_z - \dot{m} C_p T\Big|_{z+\Delta z} - U P \Delta z \left(T - T_\infty\right) = 0 \tag{31}$$

where U is the global heat transfer coefficient that groups heat transfer resistances due to conduction and convection from the bulk of the gas phase to the environment, and P the perimeter of the riser. After rearrangement and integration (with $T(0) = T_{g,in}$) the equation yields:

$$T = T_\infty + e^{-az}\left(T_{g,in} - T_\infty\right) \tag{32}$$

To estimate the parameter $a = UP/\dot{m}C_p$, the temperature T at the outlet ($z = 1.57$ m) was measured for the cases where $T_{g,in} = \{50\,°C, 100\,°C, 150\,°C\}$. In all three cases, the parameter a is similar for all conditions, and the average value is 0.67. This corresponds to a global heat transfer coefficient U of approximately 5.6, a reasonable value for a heat transfer leaded by free convection (Incropera et al., 2007). The

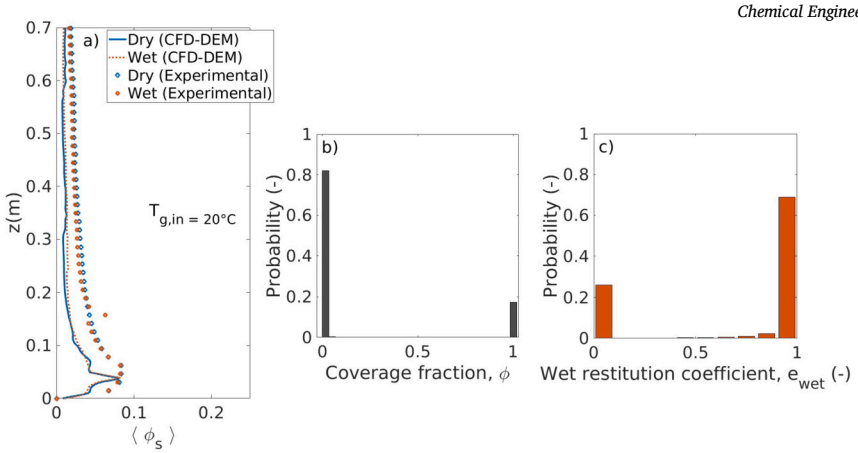

Fig. 7. Effect of liquid injection in the solid fraction distribution along the riser. a) Comparison of axial profiles of laterally-averaged solids holds up for dry and wet operation, b) probability distribution for the coverage fraction during wet operation and c) probability distribution for the restitution coefficient.

temperature profile from Equation (32) was then applied as a wall temperature condition during the simulation.

At the start of each simulation, the riser is filled with dry particles and air is injected at the desire velocity and temperature until it reaches a pseudo-steady state condition. Subsequently, the droplets are injected and the simulations are continued for 5 seconds to obtain the new pseudo-steady state. The results presented in this work are obtained by averaging over 10 seconds in this second pseudo-steady state. The different fields of interest (velocity, void fraction, temperature and moisture) are obtained every 0.05 s. In addition, the particle clusters are obtained from each void fraction field using a core-wake approach based on constant thresholds ($\varepsilon_s = 0.40$ for the core and $\varepsilon_s = 0.20$ for the wake), which is explained in detail in Ramírez et al. (2023). It should be noted that a grid resolution was performed by Carlos Varas et al. (2017b) and the current resolution has proven to be sufficient to obtain accurate results.

The CFD-DEM model used in this work is in the in-house code Foxberry (Kamath et al., 2020). All simulations are performed on a single thread of an AMD Ryzen Threadripper 2950X processing unit. The simulation time for a simulation of 1 second with 30000 particles is one day. In the current simulations, the number of particles depends largely on the liquid flow rate and the liquid coverage and ranges between 8000 and 120000.

3. Results

3.1. Solids volume fraction

Fig. 7a presents the time- and laterally-averaged axial profile of the solids volume fraction for both dry and wet condition, showing the effect of the liquid injection on the solids distribution. To ensure that only the effects of the liquid injection are studied both experiments were conducted at room temperature. Both the experiments and the simulations reflect the expected behavior of a dense bottom region of the riser that gradually becomes more diluted along the height. Comparing the experimental data during dry and wet operation, it can be concluded there is no significant effect of the liquid injection on the solids distribution, which is also predicted by CFD-DEM. Although CFD-DEM tends to under predict the solids fraction at the bottom of the riser, this difference decreases with height. A possible reason for the mismatch is a limitation of the DIA image processing method when a high solids flux is considered, since the same CFD-DEM model and riser were successfully compared in a previous study using a lower solids flux (Ramírez et al., 2023).

The small effect of the liquid injection might correspond to the high solid-to-liquid mass ratio used in this setup. This is also seen in the probability distribution of the coverage fraction of particles in Fig. 7b, as $\leq 80\%$ of the particles are virtually dry. There is a small fraction ($\sim 17\%$) of particles, which have a coverage fraction close to 1. As a consequence, the probability distribution of the restitution coefficient depicted in Fig. 7c also shows that the majority of collisions occur with a restitution coefficient of approximately the dry particles (0.96). The small portion of fully covered particles could explain the amount of collision occurring with a very low restitution coefficient. It is likely that in these collisions the liquid film is too large and/or the relative velocity between the particles too low resulting in almost all energy being dissipated during the collision.

Fig. 8a presents an evaluation of time- and laterally-averaged axial profile of the solids volume fraction for different temperatures of the injected gas. In both experiments, liquid was injected, but this is expected to have a negligible effect based on the previous results. The figure shows a small but noticeable effect of temperature on the profiles. In both experiments and simulations, the riser seems more dilute in the top of the column at higher temperatures. This is expected since the experiment at 150 °C was carried out with a significantly higher superficial gas velocity (as shown in Table 3), which has a major effect on the solids distribution inside this riser (Ramírez et al., 2023). This dilution effect is confirmed in Fig. 8b, which shows the number of particles in pseudo-steady state over time for the different temperatures. It is worth mentioning that Fig. 8a shows some peaks of solids fraction predicted by our model along the riser when $T_{g,in} = 150\,°C$. Under this condition which correspond to the highest gas velocity, the particles exhibit pneumatic behavior as they are transported up the riser. However, due to their initial injection from the left wall, the particles move upward in a zigzag pattern. This results in localized zones within the riser with consistently high solid concentrations over time, which explains the peaks in the time-averaged results.

3.2. Evaporation rate

Once the droplets are injected in the riser, they can have three different fates according to our model: i) they heat up and evaporate due to the interaction with the gas, ii) they collide and cover the surface of the solid particles, and iii) they have a splashing collision. To explore the first option the life time of the droplets before a collision was compared to the heat transfer time that leads to evaporation. It was found that $> 95\%$ of the droplets have collided within 2 ms with a particle or a wall. On the other hand, the time for heating up a droplet ($\tau = \rho_l C_{p,l} d/6h$) is on average ~ 0.9 s, suggesting that the evaporation of freely moving droplets is not the main mechanism for the disappearing of the droplets. Regarding the third mechanism (fast evaporation due to splashing), between 10-12% of the droplets had a splashing collision. This also means that the large majority of evaporation is taking place from droplets deposited on the particles' surface.

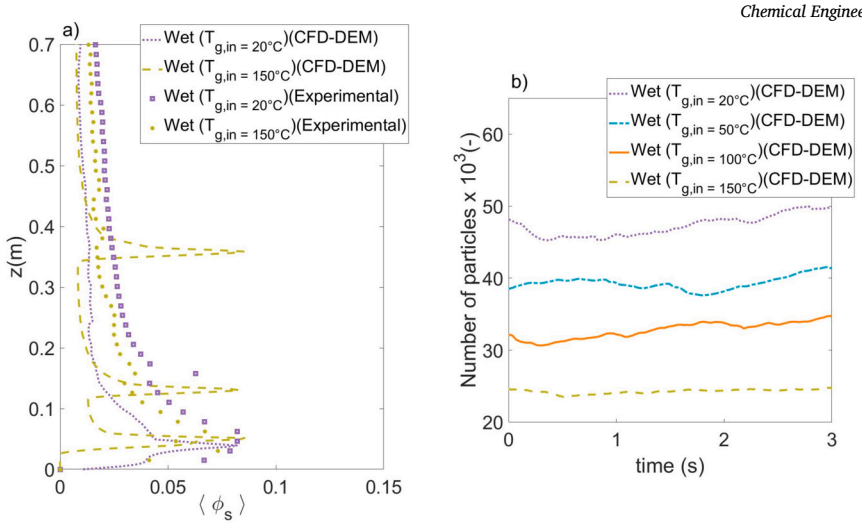

Fig. 8. Effect of temperature of the injected gas in the solids content inside the riser. a) Solids fraction distribution along the riser. b) Number of particles inside the riser in pseudo steady state as a function of time.

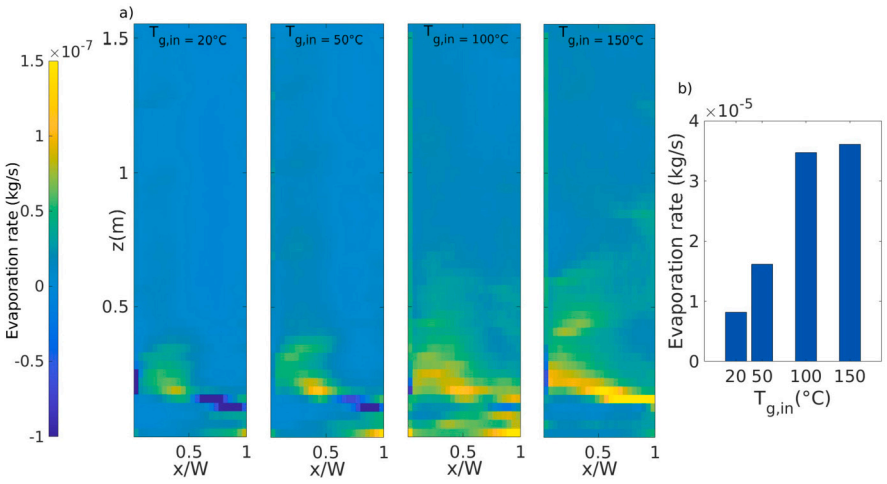

Fig. 9. Evaporation rate of the liquid deposited on the particle surface. a) Contours for the different temperature of the injected gas, b) cumulative values.

Fig. 9a presents the contours of evaporation rate for liquid deposited on the particles for different temperature conditions. It is clear that most of the evaporation occurs in the bottom region near the nozzle. The figure also shows the significant effect of the inlet temperature of the gas. Additionally, some condensation (negative values of evaporation rate) occurs near the nozzle. This might be a consequence of the high humidity caused in part by the immediate evaporation of the satellite droplets after splashing. This condensation is significantly reduced when the temperature of the gas increases. The cumulative evaporation rate from the wet particles is presented in Fig. 9b. This figure shows that the evaporation rate at a gas temperature of 150 °C is similar to the evaporation rate at 100 °C, which is caused by the higher probability of droplets colliding with the riser wall as the solid concentration is significantly reduced in this setting.

Fig. 10 presents the relative humidity contours along the riser. The figure shows that despite the high evaporation at high temperatures, the highest values of relative humidity occur at the lowest temperature, which is caused by a decreased saturation pressure at lower temperatures. The figure also shows a poor mixing in the radial direction regardless of the temperature of the gas. High values of relative humidity are primarily found near the right wall, where wet particles exhibit a high evaporation rate, as shown in Fig. 10d for the case $T_{g,in} = 150$ °C. Fig. 10 also indicates elevated humidity levels next to the left wall, caused by droplets colliding with this surface that are immediately evaporated in the model.

Fig. 11 compares the relative humidity measured at the riser outlet with the values predicted by CFD-DEM. Overall, there is a good correspondence between the curves. However, it is clear that when $T_{g,in}$ falls below 100 °C, the model shifts from overpredicting to underpredicting the relative humidity. As shown in Fig. 9, the highest condensation rates are obtained at these lower temperatures, which likely contribute to the model's lower relative humidity values. Additionally, the discrepancy between both curves may arise because the experimental values were point measurements with a humidity probe, while the simulation results represent an average over the entire outlet area (note the existence of a humidity profile at the riser outlet in Fig. 10).

3.2.1. The gas phase and solids temperature

Fig. 12 presents the time- and laterally-averaged axial temperature profile for both the gas and solids. For the gas phase, the figure also shows the measured temperature at the top of the riser, which shows a good agreement with the simulations. The figure clearly shows the heat exchange between the two phases and their approach toward thermal equilibrium along the riser height. At lower temperatures, this thermal equilibrium appears to be reached relatively quickly, whereas at the highest temperature, significant heat exchange continues beyond 1 m height.

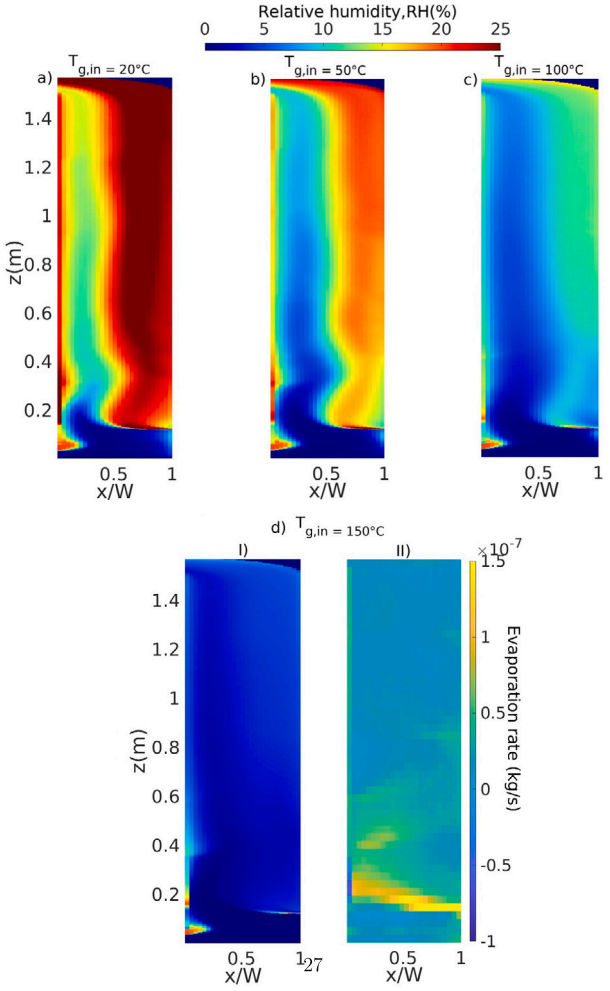

Fig. 10. Time-averaged relative humidity for the different temperatures of the injected gas. a) $T_{g,in} = 20\,°C$, b) $T_{g,in} = 50\,°C$, c) $T_{g,in} = 100\,°C$, d-I) $T_{g,in} = 150\,°C$ (accompanied by the d-II) evaporation rate of liquid deposited on the particle surface).

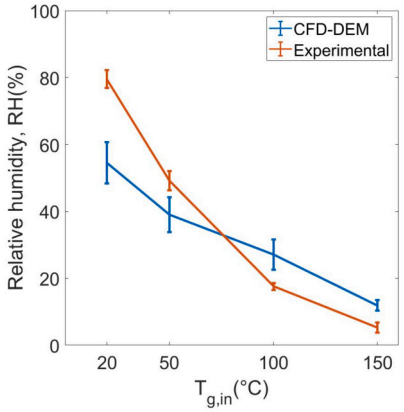

Fig. 11. Comparison of experimental and predicted relative humidity at the outlet of the riser as a function of the temperature of the injected gas.

Fig. 13 shows the time-averaged radial profiles of particle temperature at different heights. Comparing the figures from left to right, the particle temperature increases as the injected gas temperature rises. The figure also indicates that as the gas temperature increases, the difference between profiles at different heights grows. Additionally, the lowest particle temperatures are generally observed near the walls, likely due to the presence of particle clusters at the reactor walls reducing the effectiveness of the heat transfer with the gas. Note that the profiles lack radial symmetry for the highest temperatures. The larger supply of heat to the system might be revealing an asymmetric flow profile in the bottom of the riser which translates to the asymmetry in the radial profile.

Fig. 14 presents the time-averaged contours of the gas temperature. A consistent radial asymmetry is observed at the bottom of the riser, due to the injection of cold particles and air from the bottom section of the left wall.

To confirm this, Fig. 15 presents for $T_{g,in} = 150\,°C$, the gas temperature, particle temperature, and particle velocity field. It is evident that the temperature of both phases and the hydrodynamics exhibit the same behavior, which propagates more evidently for the case at the highest temperature, explaining the behavior of the particle temperature in Fig. 13d.

4. Conclusions

After experimental validation, a CFD-DEM study was conducted to investigate the heat and mass transfer occurring in a riser with liquid injection. Regarding the hydrodynamics and solids distribution, the high solid-to-liquid ratio used in this study resulted in a negligible impact of the liquid injection on the solids fraction along the riser. Instead the gas expansion at higher temperatures leads to a more diluted riser in terms of solids holdup.

The Eulerian-Lagrangian-Lagrangian approach, used to represent the gas, particles and droplets, respectively, allowed for a detailed evaluation of the droplet and evaporation mechanism. It was found that under the mild temperature conditions of this study (20 °C – 150 °C), virtually no evaporation occurs from the freely moving droplets. Instead, over 80% comes from the droplets that have collided with the particles and coat their surface. The evaporation rate is enhanced by the strong particle dynamics and high temperatures in the bottom section of the riser near the liquid injection point. Once evaporated, the vapor concentration exhibits significant radial variations, with the higher values near the wall where the nozzle is located.

This CFD-DEM enabled us to track the heat exchange progress between the gas and the particles. This showed us that especially at higher gas temperatures, significant changes in the temperatures of both phases occur even at the top of the investigated riser. Additionally, the solids circulation at the bottom of the riser is influenced by the heat exchange via the influence on the gas temperature. Finally, radial asymmetric gas temperature profiles are observed, especially at high temperatures, which are caused by the lateral feeding of the particles.

CRediT authorship contribution statement

Juan G. Ramírez: Writing – original draft, Visualization, Validation, Supervision, Software, Methodology, Investigation, Formal analysis, Data curation, Conceptualization. **Frank de Konink:** Investigation, Formal analysis, Data curation. **Vivekanand Swami:** Investigation, Formal analysis, Data curation, Conceptualization. **Maike Baltussen:** Writing – review & editing, Visualization, Validation, Supervision, Software, Methodology, Formal analysis. **Kay Buist:** Writing – review & editing, Supervision, Project administration, Methodology, Formal analysis. **Johannes A.M. (Hans) Kuipers:** Writing – review & editing, Supervision, Software, Resources, Project administration, Methodology, Formal analysis.

Declaration of generative AI and AI-assisted technologies in the writing process

During the preparation of this work the authors used ChatGPT in order to improve language and readability. After using this tool, the authors received and edited the content as needed and take full responsibility for the content of the publication.

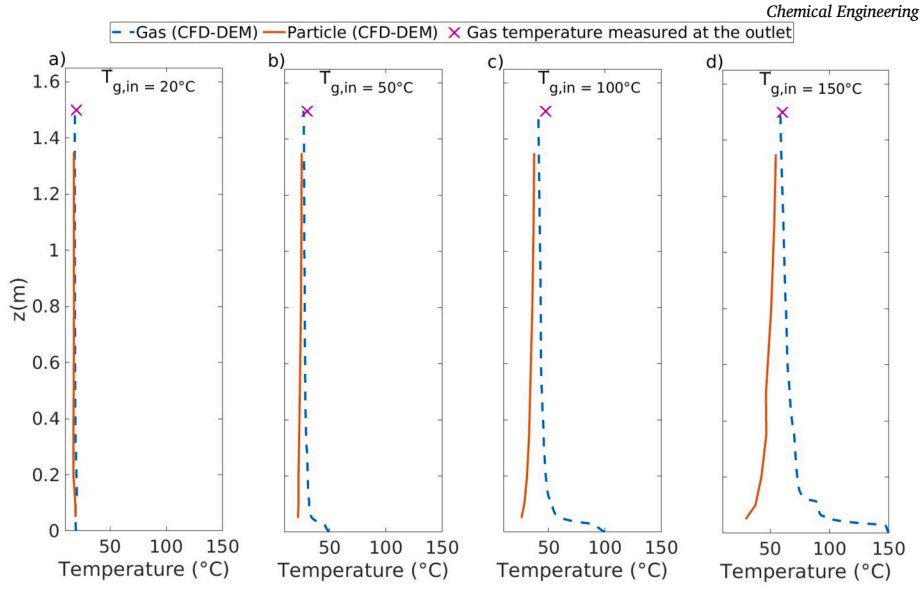

Fig. 12. Axial profiles of time- and laterally-averaged temperature for the gas and the particles. a) $T_{g,in} = 20\,°C$, b) $T_{g,in} = 50\,°C$, c) $T_{g,in} = 100\,°C$, d) $T_{g,in} = 150\,°C$.

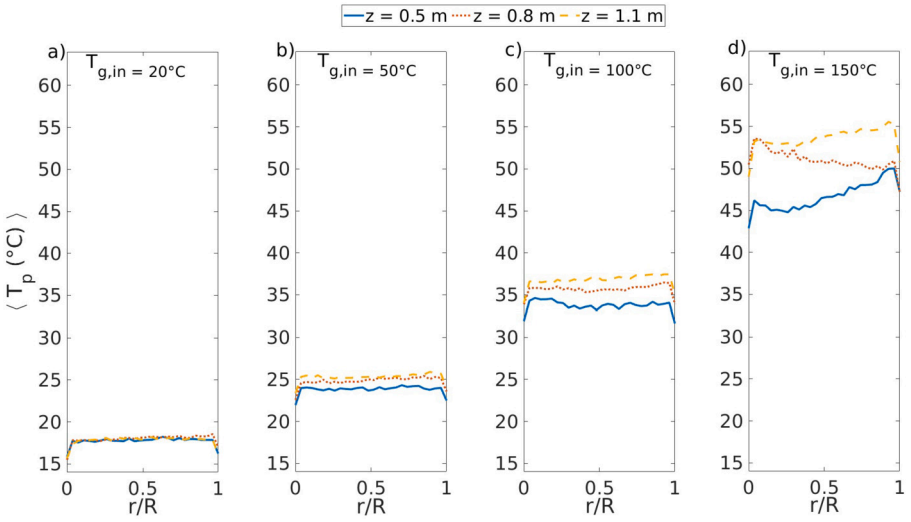

Fig. 13. The radial profiles of the time-averaged particle temperature for the different temperatures of the injected gas. a) $T_{g,in} = 20\,°C$, b) $T_{g,in} = 50\,°C$, c) $T_{g,in} = 100\,°C$, d) $T_{g,in} = 150\,°C$.

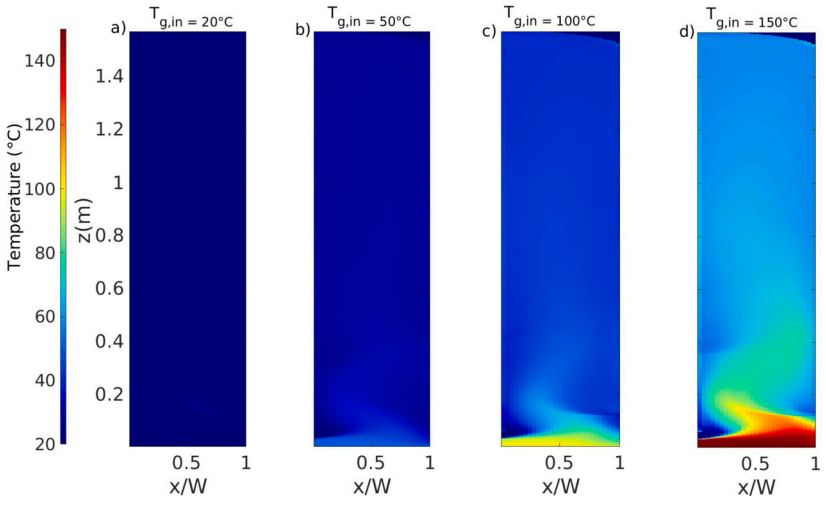

Fig. 14. Time-averaged gas temperature for the different temperatures of the injected gas. a) $T_{g,in} = 20\,°C$, b) $T_{g,in} = 50\,°C$, c) $T_{g,in} = 100\,°C$, d.I) $T_{g,in} = 150\,°C$.

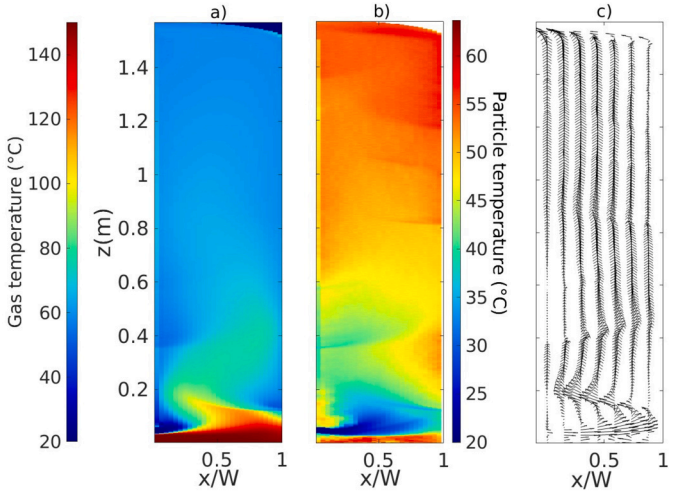

Fig. 15. Time-averaged a) gas temperature, b) particle temperature, c) particle velocity field for $T_{g,in} = 150\,°C$.

Declaration of competing interest

The authors declare the following financial interests/personal relationships which may be considered as potential competing interests: J.A.M. Kuipers reports financial support was provided by Netherlands Center for Multiscale Catalytic Energy Conversion (MCEC). If there are other authors, they declare that they have no known competing financial interests or personal relationships that could have appeared to influence the work reported in this paper.

Acknowledgement

This work was supported by the Netherlands Center for Multiscale Catalytic Energy Conversion (MCEC), an NWO Gravitation programme funded by the Ministry of Education, Culture and Science of the government of the Netherlands.

This research has received funding from the European Union's Horizon 2020 research and innovation programme under the Marie Skłodowska-Curie grant agreement No. 801359.

Appendix A. Supplementary material

Supplementary material related to this article can be found online at https://doi.org/10.1016/j.ces.2024.121066.

Data availability

Data will be made available on request.

References

Ali, H., Rohani, S., Corriou, J.P., 1997. Modelling and control of a riser type fluid catalytic cracking (FCC) unit. Chem. Eng. Res. Des. 75, 401–412.

Anzelius, A., 1926. Uber erwarmung vermittels durchstromender medien. J. Appl. Math. Mech. 6, 291–294.

Ben, Freireich, Wassgren, Carl, 2010. Intra-particle coating variability: analysis and Monte-Carlo simulations. Chem. Eng. Sci. 65, 1117–1124.

Buchanan, J. Scott, 1994. Analysis of heating and vaporization of feed droplets in fluidized catalytic cracking risers. Ind. Eng. Chem. Res. 33, 3104–3111.

Carlos Varas, A.E., Peters, E.A.J.F., Kuipers, J.A.M., 2017a. Experimental study of full field riser hydrodynamics by PIV/DIA coupling. Powder Technol. 313, 402–416.

Carlos Varas, A.E., Peters, E.A.J.F., Kuipers, J.A.M., 2017b. CFD-DEM simulations and experimental validation of clustering phenomena and riser hydrodynamics. Chem. Eng. Sci. 169, 246–258.

Cundall, P.A., Strack, O.D.L., 1979. A discrete numerical model for granular assemblies. Géotechnique 29 (1), 47–65.

Derouin, Céline, Nevicato, David, Forissier, Michel, Wild, Gabriel, Bernard, Jean-René, 1997. Hydrodynamics of riser units and their impact on FCC operation. Ind. Eng. Chem. Res. 36 (11), 4504–4515.

Fan, L.-S., Lau, R., Zhu, C., Vuong, K., Warsito, W., Wang, X., Liu, G., 2001. Evaporative liquid jets in gas-liquid-solid flow system. Chem. Eng. Sci. 56, 5871–5891.

Gao, Jinsen, Xu, Chunming, Lin, Shixiong, Yang, Guanghua, Guo, Yincheng, 2001. Simulations of gas-liquid-solid 3-phase flow and reaction in FCC riser reactors. AIChE J. 47, 677–692.

Gehrke, S., Wirth, K.E., 2007. Liquid feed injection in a high density riser. In: The 12th International Conference on Fluidization. http://dc.engconfintl.org/fluidization_xii/8.

Gunn, D.J., 1978. Transfer of heat or mass to particles in fixed and fluidised beds. Int. J. Heat Mass Transf. 21 (4), 467–476.

Gupta, Ajay, Subba Rao, D., 2001. Model for the performance of a fluid catalytic cracking (FCC) riser reactor: effect of feed atomization. Chem. Eng. Sci. 56, 4489–4503.

Hoomans, B.P.B., Kuipers, J.A.M., Briels, W.J., van Swaaij, W.P.M., 1996. Discrete particle simulation of bubble and slug formation in a two-dimensional gas-fluidised bed: a hard-sphere approach. Chem. Eng. Sci. 51 (1), 99–118.

Incorporated American Society of Heating, Refrigerating & Air Conditioning Engineers, 2001. ASHRAE Fundamentals Handbook 2001 (SI). American Society of Heating, Refrigerating & Air Conditioning Engineers, Incorporated.

Incropera, Frank P., Dewitt, David P., Bergman, Theodore L., Lavine, Adrienne S., 2007. Fundamentals of Heat and Mass Transfer, 6th edition.

Kamath, S., Masterov, M.V., Padding, J.T., Buist, K.A., Baltussen, M.W., Kuipers, J.A.M., 2020. Parallelization of a stochastic Euler-Lagrange model applied to large scale dense bubbly flows. J. Comp. Phys. X 8.

Kariuki, Waithira I.J., Freireich, Ben, Smith, Rachel M., Rhodes, Martin, Hapgood, Karen P., 2013. Distribution nucleation: quantifying liquid distribution on the particle surface using the dimensionless particle coating number. Chem. Eng. Sci. 92, 134–145.

Lopes, Gabriela C., Rosa, Leonardo M., Mori, Milton, Nunhez, José R., Martignoni, Waldir P., 2012. CFD study of industrial FCC risers: the effect of outlet configurations on hydrodynamics and reactions. Int. J. Chem. Eng. 2012, 193639.

Muzychka, Y., Yovanovich, M., 1998. Modeling Nusselt numbers for thermally developing laminar flow in non-circular ducts. In: AIAA 1998-2586. 7th AIAA/ASME Joint Thermophysics and Heat Transfer Conference.

Patel, H.V., Das, S., Kuipers, J.A.M., Padding, J.T., Peters, E.A.J.F., 2017. A coupled volume of fluid and immersed boundary method for simulating 3d multiphase flows with contact line dynamics in complex geometries. Chem. Eng. Sci. 166, 28–41.

Ramírez, J., de Munck, M.J.A., Liu, Z., Rieder, D.R., Baltussen, M.W., Buist, K.A., Kuipers, J.A.M., 2023. CFD-DEM evaluation of the clustering behavior in a riser the effect of the drag force model. Ind. Eng. Chem. Res. 62 (45), 18960–18972.

Ramírez, J., Peene, L., Baltussen, M.W., Buist, K.A., Kuipers, J.A.M., 2024. Three-phase CFD-DEM study on the hydrodynamics of a riser system with liquid injection. Chem. Eng. J. 501, 157449.

Shabanian, Jaber, Duchesne, Marc A., Runstedtler, Allan, Syamlal, Madhava, Hughes, Robin W., 2020. Improved analytical energy balance model for evaluating agglomeration from a binary collision of identical wet particles. Chem. Eng. Sci. 223, 115738.

Shah, Milinkumar T., Utikar, Ranjeet P., Pareek, Vishnu K., Evans, Geoffrey M., Joshi, Jyeshtharaj B., 2016. Computational fluid dynamic modelling of FCC riser: a review. Chem. Eng. Res. Des. 111, 403–448.

Stull, Roland, 2011. Wet-bulb temperature from relative humidity and air temperature. J. Appl. Meteorol. Climatol. 50, 2267–2269.

Sutkar, Vinayak S., Deen, Niels G., Padding, Johan T., Kuipers, J.A.M., Salikov, Vitalij, Crüger, Britta, Antonyuk, Sergiy, Heinrich, Stefan, 2015. A novel approach to determine wet restitution coefficients through a unified correlation and energy analysis. AIChE J. 61, 769–779.

Sutkar, Vinayak S., Deen, Niels G., Patil, Amit V., Salikov, Vitalij, Antonyuk, Sergiy, Heinrich, Stefan, Kuipers, J.A.M., 2016. CFD-DEM model for coupled heat and mass transfer in a spout fluidized bed with liquid injection. Chem. Eng. J. 288, 185–197.

Tang, Y., Kriebitzsch, S.H.L., Peters, E.A.J.F., Kuipers, J.A.M., van der Hoef, M.A., 2015. A new drag correlation from fully resolved simulations of flow past monodisperse static arrays of spheres. AIChE J. 61, 688–698.

Theologos, K.N., Lygeros, A.I., Markatos, N.C., 1999. Feedstock atomization effects on FCC riser reactors selectivity. Chem. Eng. Sci. 54, 5617–5625.

Tsuji, Y., Tanaka, T., Yonemura, S., 1998. Cluster patterns in circulating fluidized beds predicted by numerical simulation (discrete particle model versus two-fluid model). Powder Technol. 95, 254–264.

Yoon, Ikroh, Shin, Seungwon, 2021. Direct numerical simulation of droplet collision with stationary spherical particle: a comprehensive map of outcomes. Int. J. Multiph. Flow 135, 103503.